



HAL
open science

Barite precipitation in porous media: Impact of pore structure and surface charge on ionic diffusion

A. Rajyaguru, J. Wang, C. Wittebroodt, O. Bildstein, V. Detilleux, Vincent Lagneau, S. Savoye

► **To cite this version:**

A. Rajyaguru, J. Wang, C. Wittebroodt, O. Bildstein, V. Detilleux, et al.. Barite precipitation in porous media: Impact of pore structure and surface charge on ionic diffusion. *Journal of Contaminant Hydrology*, 2021, 242, pp.103851. 10.1016/j.jconhyd.2021.103851 . hal-03313533

HAL Id: hal-03313533

<https://minesparis-psl.hal.science/hal-03313533>

Submitted on 2 Aug 2023

HAL is a multi-disciplinary open access archive for the deposit and dissemination of scientific research documents, whether they are published or not. The documents may come from teaching and research institutions in France or abroad, or from public or private research centers.

L'archive ouverte pluridisciplinaire **HAL**, est destinée au dépôt et à la diffusion de documents scientifiques de niveau recherche, publiés ou non, émanant des établissements d'enseignement et de recherche français ou étrangers, des laboratoires publics ou privés.



Distributed under a Creative Commons Attribution - NonCommercial 4.0 International License

Barite precipitation in porous media: impact of pore structure and surface charge on ionic diffusion

A. Rajyaguru^{1,2*}, J. Wang¹, C. Wittebroodt³, O. Bildstein⁴, V. Detilleux⁵, V. Lagneau², S. Savoye¹

(1) DES-ISAS-Service d'Etude du Comportement des Radionucléides (SECR), CEA, Université Paris-Saclay, F-91191 Gif-sur-Yvette

(2) MINES Paris-Tech, Centre de Géosciences, France

(3) IRSN, LETIS, Fontenay Aux Roses, France

(4) CEA, DES, IRESNE, DTN, Laboratory for Modeling of Transfers in the Environment, F-13108 Saint Paul-lez-Durance, France

(5) Bel V, Belgium

*Corresponding author: Ashish RAJYAGURU

Paul Scherrer Institut

WLGA/211

Forschungsstrasse 111

5232 Villigen PSI

Switzerland

email: ashish.rajyaguru@psi.ch

19 **Abstract:** Several scientific fields such as global carbon sequestration, deep geological
20 radioactive waste disposal, and oil recovery/fracking encounter safety assessment issues
21 originating from pore-scale processes such as mineral precipitation and dissolution. These
22 processes occur in situations where the pore solution contains chemical complexity (such as pH,
23 ionic strength, redox chemistry, etc...) and the porous matrix contains physical complexity (such
24 as pore size distribution, surface charge, surface roughness, etc...). Thus, to comprehend the
25 participation of each physicochemical phenomenon on governing mineral precipitation, it is
26 essential to investigate the precipitation behavior of a given mineral in different confined
27 volumes. In this study, a counter-diffusion approach was used to investigate barite precipitation
28 in two porous materials: micritic chalk and compacted kaolinite. The two materials present
29 similar water and anionic tracer diffusivities and total accessible porosities but distinct pore size
30 distributions with pore throats of c.a. 660 nm in chalk *versus* c.a. 35 nm in kaolinite.

31 X-ray tomography results obtained on the two materials showed a distinct distribution of barite
32 precipitates: a 500 μm -thick homogeneous layer in chalk *versus* spherical clusters spread in a
33 thickness of 2 mm in kaolinite. Mass balance calculations showed that barite precipitation led to a
34 porosity decrease in the chalk reacted zone from 45 % to 12 % and in the kaolinite reacted zone
35 from 36 % to 34.5 %. In contrast, water tracer diffusion experiments showed that diffusivity
36 decreased by a factor of 28 in chalk and by a factor of 1000 in kaolinite. Such a discrepancy was
37 attributed to the difference in the pore size distribution that would lead to the distinct barite
38 precipitation patterns, capable of altering in a very different manner the connectivity within the
39 reacted zone of the two selected porous media.

40 Such local alterations in connectivity linked to pore volume reduction would also magnify
41 surface charge effects on ionic transport, as indicated by chloride diffusion experiments and
42 electrophoretic tests using zeta potential measurements. Indeed, $^{36}\text{Cl}^-$ was strongly more hindered
43 than water, when diffused in reacted materials, with a diffusivity decrease by a factor of 450 in
44 chalk and a total restriction of $^{36}\text{Cl}^-$ in kaolinite. These experiments clearly provide an insight of
45 how local pore structure properties combined with mineral reactivity could help in predicting the
46 evolution of pore scale clogging and its impact on water and ionic diffusive transport.

47

48 **Keywords:**

49 diffusion; precipitation; chalk; kaolinite; barite; surface charge; pore structure.

50 1. INTRODUCTION

51 In France, Switzerland and Belgium, argillaceous rock formations are considered potential host
52 rocks for radioactive waste disposal facilities (Gaucher *et al.*, 2004; NAGRA, 2002). Similar
53 indurated rocks are also envisaged as cap rocks to seal anthropogenic CO₂ reservoirs for global
54 carbon sequestration (GCS) (Bachu, 2002; Berthe *et al.*, 2011; Fleury and Brosse, 2018). These
55 rocks are selected due to their low permeabilities, which makes diffusion the main mass transport
56 process, and their high concentrations of clay minerals, whose negatively charged surfaces are
57 capable of adsorbing radionuclides under cationic form (Andra, 2005). However, the degradation
58 of radioactive waste in disposal facilities and similarly, the use of different trapping methods to
59 capture CO₂ in reservoir rock may generate some physicochemical imbalances that can enhance
60 mineral dissolution and/or precipitation processes. Since these processes change the mineral
61 composition of rock matrix, they can potentially alter the rock containment properties (Dagnelie
62 *et al.*, 2017; De Windt *et al.*, 2008) and lead to safety assessment issues.

63 Assessments of the long-term evolution of rock containment properties are generally performed
64 using numerical chemistry transport codes. In these codes, the porosity change is estimated from
65 mineralogical volume balance due to precipitation/dissolution. Feedback on diffusivity is then
66 determined by the empirical Archie's relationship, which links the change in diffusivity to the
67 porosity changes, *i.e.* $\frac{D_e}{D_o} = \phi^m$, where D_e is the effective diffusive coefficient in m² s⁻¹, D_o is the
68 diffusion coefficient in bulk water in m² s⁻¹, ϕ is the total porosity of the porous sample, and m
69 is a fitting factor also known as the cementation factor (Archie, 1942). However, very few lab-
70 scale experiments are available to assess the validity of this relationship when used in numerical
71 models that couple changes in transport process with mineral reactivity (*i.e.* chemical interactions
72 and diffusive processes) *via* strong porosity changes (Chagneau *et al.*, 2015a; Rajyaguru *et al.*,

73 2019). Recently, Rajyaguru *et al.* (2019) showed that the distinct precipitation behavior of barite
74 and gypsum in a chalk sample led to a very different impact on the diffusivity of a water tracer.
75 The authors noted that this difference in precipitation behavior stems from the combined effect of
76 mineral intrinsic properties (solubility, precipitation rate) and spatial variability in the properties
77 of chalk (pore structure, reactive surface). Similarly, Singurindy and Berkowitz (2003) studied
78 calcite dissolution by sulfuric acid and hydrochloric acid solutions and gypsum re-precipitation in
79 a compacted sand matrix. This study showed that the flow rate and concentration of acid in the
80 injected solution controlled the pattern of calcite dissolution channels and gypsum morphology.
81 Other studies outlined that nucleation phenomena governed local mineral growth (Poonoosamy *et al.*
82 *et al.*, 2016; Prieto, 2014), that pore pressure controlled crystal stability in confined media (Putnis
83 and Mauthe, 2001; Rijniers *et al.*, 2005), and that both processes collectively defined the
84 possibility of precipitation in a given pore class (Emmanuel *et al.*, 2010). One could infer from
85 these studies that the nature of precipitation and its feedback on diffusion is potentially governed
86 by the pore size distribution of the hosted material than by the porosity (volume of void) itself,
87 contrary to the paradigm of the widely used Archie's law.

88 These studies also outline that local mineral distribution and morphology can be used to
89 qualitatively decipher the average change in intrinsic properties of a reacted sample. Furthermore,
90 formation of secondary mineral surfaces could also generate surface charge effects that were not
91 visible in a porous material under intact form. In this case, ionic species diffusivity may differ
92 from that of neutral species, such as a water tracer. Depending upon pH, electrolyte
93 concentration, and the presence of potential determining ions, the sulfate alkali minerals may
94 possess varying amounts of negative or positive surface charges (González-Caballero *et al.*,
95 1988; Hang *et al.*, 2009). For instance, Chagneau *et al.* (2015b) investigated the impact of
96 celestite precipitation on transport properties through compacted illite. The authors showed that

97 the reacted zone in illite allowed water tracer to diffuse, whereas $^{36}\text{Cl}^-$ diffusion was completely
98 restricted. They proposed that the presence of additional negative surface charges on celestite,
99 combined with surface charges on illite, resulted in total porosity clogging and restriction of
100 $^{36}\text{Cl}^-$ diffusion through the reacted zone (Chagneau *et al.*, 2015b). All of these experimental and
101 theoretical observations indicate that reactive transport in porous media is a process that strongly
102 couples chemical reactivity of minerals with local transport properties of the host pore structure.

103 The objective of the present work is twofold. The first goal is to experimentally investigate the
104 role of pore size distribution on barite precipitation in two reference porous media having similar
105 initial diffusive properties but distinct pore size distributions: chalk and compacted kaolinite.
106 Barite was chosen as its formation is of concern in geothermal reservoirs and hydraulic fracturing
107 (Mundhenk *et al.*, 2013; Vengosh *et al.*, 2014) and as it is capable of trapping radium in mill
108 tailings of former uranium mines (Besançon *et al.*, 2020; Chautard *et al.*, 2020) and in nuclear
109 waste disposal facilities (Brandt *et al.*, 2018; Vinograd *et al.*, 2018). The second objective is to
110 quantify the impact of barite precipitates on diffusive transport properties. Neutral species
111 (tritiated water) and ionic species ($^{36}\text{Cl}^-$) were used as reference tracers, since both the barite
112 precipitates and the host pore surfaces were charged and therefore expected to generate a
113 combined surface charge effect that could govern ionic species transport through the reacted
114 samples. Results from these experiments may be used to improve safety assessments tests in sites
115 of nuclear waste disposal and/or carbon sequestration, where robust numerical models are needed
116 to predict the change in ionic transport properties (diffusivity) through host rocks in response to
117 local clogging.

118 **2. MATERIALS AND METHODS**

119 **2.1. Sample Preparation and Characterization**

120 Kaolinite KGa-2 clay powder with particle size $\sim 150 \mu\text{m}$ was provided by CNRS-Poitiers
121 University. This clay was saturated with Na using five saturation cycles in a 1 mol L^{-1} NaCl
122 solution and a dialysis procedure was used to remove chloride from the samples until the silver
123 nitrate test for Cl^- was negative. Then, each size fraction was air dried, sieved through a 50-
124 μm mesh to remove coarse aggregates, and stored at 25°C .

125 Chalk samples were selected from Upper Cretaceous formations belonging to the chalk aquifer
126 of the Paris Basin in the Champagne region (France) (Descostes *et al.*, 2012; Rajyaguru *et al.*,
127 2019). The samples were derived from a core section (85 mm diameter) of a borehole that
128 crossed the Lower Campanian-age stratigraphic layer (approximately 83 My). The extracted core
129 was then sliced into 0.67 cm-thick and 3.3 cm-diameter slices perpendicular to the bedding plane
130 using a diamond wire saw (no lubricating fluid was used).

131 Mercury intrusion and extrusion porosimetry (MIEP) characterization was carried out both on
132 Na-kaolinite compacted at a dry density of 1690 kg m^{-3} and a chalk sample using a
133 Micromeritics Autopore III 9420 apparatus. The total porosity and the mean pore throat derived
134 from this analysis were 36 % and 35 nm, respectively, for kaolinite and 45 % and 660 nm for
135 chalk.

136 **2.2. Experimental setup used for kaolinite and chalk**

137 A schematic representation of the diffusion cell connected to two reservoirs used in kaolinite
138 study is represented in Figure-S1 in supporting information. The through diffusion setup
139 developed by Tertre *et al.* (2018) was used for studying precipitation in the kaolinite sample. This
140 setup consists of a diffusion cell made of Polyetheretherketone (PEEK) and characterized by an
141 inner diameter of 9.49 mm and two aqueous counter reservoirs (*i.e.*, an upstream reservoir and a
142 downstream reservoir). The compacted kaolinite sample were prepared by a direct compaction in

143 the diffusion cell at a bulk dry density of 1690 kg m^{-3} based on the dry mass of the solid placed
144 in the cell and the volume of the cell, leading to a sample thickness of 10 mm.

145 Three porous layers were placed on each face of the sample ; they were composed of 1)
146 Whatman cellulose nitrate membrane filters (manufactured by GE Healthcare) of $0.8 \mu\text{m}$ mesh,
147 2) Stainless-steel filter plates (pore diameter $10 \mu\text{m}$ from the Mott industrial division), and 3)
148 Two grids (nominal spaces of $280 \mu\text{m}$ and $450 \mu\text{m}$ for monofilaments with diameters equal to
149 $120 \mu\text{m}$ and $200 \mu\text{m}$, respectively, from Goodfellow). These porous layers ensure homogeneous
150 solution supply at each face of the sample.

151 The air from the sample pore space was replaced with pore water using ascendant capillary
152 method in a vertically standing positioned diffusion cell. In this method, the downstream face
153 was kept under vacuum by connecting the inlet and outlet holes to a vacuum pump.
154 Simultaneously, at upstream the inlet was connected to nitrogen pentoxide gas bottle, while the
155 outlet was connected to a 0.1 M NaCl solution reservoir using a peristaltic pump. The vacuum
156 pump and nitrogen pentoxide were disconnected once solution from upstream reached the
157 downstream face. Both faces were then connected to two reservoirs containing 0.1 M NaCl
158 solution, and an equilibration process of two weeks was initiated to ensure an ionic charge
159 balance between the reservoir electrolytes and the pore solution.

160 For the current study, the first diffusion cell labeled KAO-A was used to acquire diffusion
161 parameters for tritiated water (HTO) and $^{36}\text{Cl}^-$ through kaolinite before and after the reactive
162 diffusion experiment. The second cell, labeled KAO-B, was used to determine the 3D evolution
163 of barite precipitates in the kaolinite pore network 30 days and 60 days after the start of the
164 reactive diffusion experiment using X-ray microtomography investigation.

165 The barite precipitation experiments in chalk were carried out using a static diffusion cell as
166 developed by Descostes *et al.* (2012). In this setup, the chalk sample was sandwiched between

167 upstream and downstream reservoirs with volumes of 178 mL and 140 mL, respectively (a
168 schematic view is reported in Figure-S2 in supporting information). A sample holder held the
169 sandwiched sample and all the parts (upstream reservoir, sample, sample holder, and downstream
170 reservoir) were assembled, glued and screwed together to generate a complete through-diffusion
171 cell. Two similar cells were prepared: one for the determination of the radioactive tracer's
172 diffusive behavior through intact and reacted chalk (labeled CHA-A) and the second one for the
173 postmortem characterization of reacted chalk by X-ray microtomography and SEM observations
174 (labeled CHA-B). The details on the preparation of the cell, the equilibration step and the
175 concentration of ions in reservoir solutions can be found in (Rajyaguru *et al.*, 2019).

176 **2.3. Barite precipitation in chalk and kaolinite**

177 In kaolinite sample, precipitation was launched by replacing the upstream reservoir solution
178 with 20 mL of fresh 100 mmol L⁻¹ NaCl solution containing 4 mmol L⁻¹ of BaCl₂ and, similarly,
179 the downstream reservoir solution was replaced with 20 mL of 100 mmol L⁻¹ NaCl solution
180 containing 4 mmol L⁻¹ Na₂SO₄. The upstream solution was spiked with 25 μL of ¹³³Ba (source
181 ELSB45 CERCA n°5245 with an activity of 1.78 MBq L⁻¹). Using the initial ratio of stable
182 barium concentration and ¹³³Ba activity in upstream, the sampled activities were converted into
183 stable barium concentrations. For this operation, 100 μL of the upstream solution was
184 periodically sampled and mixed with 900 μL of ultrapure water. The activity measurement was
185 determined using a gamma counter (Packard 1480 WIZARD). Similarly, sulfate concentration
186 was measured using ionic chromatography (Dionex 500 equipped with an AS14 IonPac column)
187 in 100 μL of sampled downstream solution and diluted in 900 μL of ultrapure water.

188 For the chalk experiments, the upstream reservoir was filled with a chalk-equilibrated solution
189 (*i.e.* 160 mmol L⁻¹ of NaCl, 20 mmol L⁻¹ of CaCl₂, and 0.4 mmol L⁻¹ of NaHCO₃) containing

190 20 mmol L⁻¹ of BaCl₂ (downstream reservoir with 20 mmol L⁻¹ Na₂SO₄). The reservoir
191 monitoring protocol described for the kaolinite case was also used for chalk to obtain barium and
192 sulfate concentration evolution throughout the duration of the experiments. A detailed
193 information of reservoirs solution chemistry obtained by (Rajyaguru *et al.*, 2019) is reported in
194 Table-S1 in supporting information.

195 For both sample types, the aim of periodic chemistry monitoring was to determine the time at
196 which reactants achieve quasi-equilibrium state in their respective reservoir. Such information is
197 required to calculate the total barite amount having precipitated in samples and the time at which
198 tracer diffusivity tests for reacted samples could be initiated.

199 One must note that, in the rest of the article, reservoirs labelled as upstream and downstream
200 reservoir are used to distinguish barium and sulfate reservoirs and do not bear any advective
201 meaning.

202 **2.4. Postmortem 3D imaging (μ CT)**

203 3D views of the barite-precipitated zones in the kaolinite and chalk samples were obtained by
204 performing X-ray microtomography (μ CT) on the cells KAO-B and cell CHA-B. Both cells had
205 similar experimental conditions (reactant concentration, volume of reservoirs, sample geometry)
206 as KAO-A and CHA-A cells.

207 For the kaolinite experiment, after 30 days and 60 days since starting of the reactive diffusion
208 experiment, the circulation of reactants in KAO-B was temporarily stopped for 1 day. The whole
209 diffusion cell was disconnected from the reservoirs and placed in an X-ray microtomography
210 (μ CT) apparatus. After tomography imaging, the cell was connected back to the reservoirs to
211 continue the barite precipitation process. In the case of chalk, the size of the experimental setup
212 prevented any μ CT imaging during the experiment. Thus, CHA-B cell was dismantled after 140

213 days, and barite-precipitated chalk sample was removed from the supporting ring and then used
214 for imaging.

215 For both studies, a Skyscan 1272 microtomography apparatus (Bruker) was used to acquire
216 images. The μ CT images for the kaolinite and chalk samples were compared to determine the
217 formation of a precipitated zone in compacted porous media (kaolinite) and natural porous media
218 (micritic chalk). In kaolinite, the maximal spatial resolution of reacted zone was 16 μm due to
219 sample size. In chalk, a piece of reacted zone considered as a representative elementary volume
220 was imaged with a spatial resolution of 1 μm .

221 **2.4. Tracers' through diffusion tests**

222 For the kaolinite sample, after the equilibration step of KAO-A sample (explained in section
223 2.2), the upstream reservoir solution was completely replaced with 100 mL of fresh solution with
224 100 mmol L^{-1} of NaCl. This reservoir was spiked with 180 μL of tritiated water (labeled
225 CERCA ELSB45 n°760112/4) and 65 μL of $^{36}\text{Cl}^-$ (labeled E&Z 1760-100-1) to achieve
226 volumetric activities of 1 MBq L^{-1} for HTO and 0.5 MBq L^{-1} for $^{36}\text{Cl}^-$. Similarly, the
227 downstream reservoir solution was replaced with 10 mL of fresh solution with 100 mmol L^{-1} of
228 NaCl. To ensure a constant activity gradient between both reservoirs, the downstream solution at
229 each sampling was renewed with 10 mL of fresh solution. The protocol to measure tracer activity
230 is as follows: 100 μL of the sampled solutions were mixed with 900 μL of ultrapure water and
231 4 mL of Ultima Gold scintillation liquid in a 5 mL scintillation bottle. The activities were
232 measured using a Packard Tri-Carb 2500 liquid scintillation recorder. Once tracer diffusivity was
233 obtained at intact condition, the tracers were out diffused from sample pore solution by replacing
234 both reservoirs with 100 mL of tracer-free solution for two weeks.

235 Using reservoir-monitoring step described in section 2.3., the reactant quasi-equilibrium step
236 was achieved after 85 days since the beginning of experiment. At this stage HTO and $^{36}\text{Cl}^-$
237 tracers with volumetric activities similar to the intact case (1 MBq L^{-1} for HTO and 0.5 MBq L^{-1}
238 $^{36}\text{Cl}^-$) were directly injected into the upstream solution. This step ensured that similar initial
239 tracers' activity values were achieved for pure diffusion and reactive diffusion step. In the
240 reactive diffusion experiment, as the diffusive parameters were estimated under ongoing
241 precipitation process, a careful direct injection of tracer in upstream solution was done to ensure
242 no disturbance of solution chemistry. Similarly, the downstream solution at each sampling was
243 not renewed (contrary to intact case), but the activity change was directly measured by a periodic
244 withdrawal of $100 \mu\text{L}$ of solution from the reservoir. One must note that the protocol for activity
245 measurement using liquid scintillation recorder is the same as the protocol used at intact
246 conditions.

247 For chalk, water tracer diffusivity in an intact sample has already been reported in Rajyaguru *et*
248 *al.* (2019). The barite precipitation process in cell CHA-A was continued for a total experimental
249 time of 300 days (one must note that the chemistry monitoring in this experiments was done only
250 for 140 days). At this stage, the upstream solution was directly spiked with HTO (labeled
251 CERCA ELSB45 n°760112/4) and $^{36}\text{Cl}^-$ (labeled E&Z 1760-100-1) to achieve volumetric
252 activities of 0.40 MBq L^{-1} for HTO and 0.30 MBq L^{-1} for $^{36}\text{Cl}^-$, respectively. The protocol
253 used for the measurement of the activity consisted of mixing 4 mL of Ultima Gold scintillation
254 liquid with either $50 \mu\text{L}$ of the upstream solution plus $900 \mu\text{L}$ of ultrapure water or 1 mL of the
255 downstream solution in a 5 mL scintillation bottle. One milliliter of tracer-free solution was
256 added in the downstream reservoir of the chalk cell at each sampling to keep the volume of the
257 downstream reservoir constant.

258 For kaolinite and chalk, HTO and $^{36}\text{Cl}^-$ diffusive parameters values in intact and reacted
259 conditions were estimated by a numerical fitting of the activity data using I-mode (see next
260 section).

261 **2.5. Treatment of the experimental diffusive results**

262 The experimental activity datasets for both HTO and $^{36}\text{Cl}^-$ were interpreted numerically using
263 Fick's second law for one-dimensional transport (Crank, 1975):

$$264 \quad \frac{\partial C}{\partial t} = \frac{D_e}{\alpha} \frac{\partial^2 C}{\partial x^2} = \frac{D_e}{\varepsilon + R_d \rho_{app}} \frac{\delta^2 C}{\delta x^2} \quad (1)$$

265 where C is the concentration in mol m^{-3} (or activity Bq m^{-3} in our case), t is the time in s, D_e
266 is the effective diffusion coefficient in $\text{m}^2 \text{s}^{-1}$, $\alpha = \varepsilon + R_d \rho_{app}$ is the rock capacity factor, ε is the
267 porosity, ρ_{app} is the bulk dry density in kg m^{-3} , and R_d is the distribution ratio in $\text{m}^3 \text{kg}^{-1}$. The
268 initial and boundary conditions for this through-diffusion setup when the concentration in
269 upstream and downstream reservoirs is left to freely evolve are as follows:

$$270 \quad C(x,t) = 0 \text{ for } t = 0 \quad (2)$$

$$271 \quad C(x,t) = C_0 \text{ for } x = 0 \text{ at } t = 0 \quad (3)$$

$$272 \quad C(x,t) = 0 \text{ for } x = L + 2l \text{ at } t = 0 \quad (4)$$

273 where C_0 is the initial concentration (or initial activity in Bq m^{-3}) in the upstream reservoir at
274 the injection time, L is the sample thickness (m) and l is the filter plate thickness (m). The total
275 porosity and effective diffusion coefficient of these filter plates only used in the kaolinite
276 diffusion cells, equal to 28% and $2.3 \times 10^{-10} \text{ m}^2 \text{ s}^{-1}$, respectively, for HTO and $2.0 \times 10^{-10} \text{ m}^2 \text{ s}^{-1}$
277 for $^{36}\text{Cl}^-$, are taken from the literature (Tertre *et al.*, 2018). Using the initial and boundary
278 conditions from equations 2, 3 and 4, semi-analytical solutions to determine the cumulative
279 activity in downstream reservoirs are given in literature by Didierjean *et al.* (2004). The semi-

280 analytical solutions were implemented in CEA's Interpretation Model of Diffusion Experiments
281 (I-Mode) tool (Radwan *et al.*, 2006).

282 For the through-diffusion setup, the associated errors in the measured cumulative activities in
283 the downstream reservoirs were calculated using the Gaussian error propagation method. The
284 mathematical equation for this operation was taken from Bazer-Bachi *et al.* (2006). These
285 equations are detailed in the supporting information.

286 Note that the HTO and $^{36}\text{Cl}^-$ diffusive data obtained on reacted samples were also interpreted
287 using this simplified description of the current experimental system (e.g. one dimensional
288 transport, charge induced mechanisms not taken into account). In this case, the limitations related
289 to this modelling approach were acknowledged, assuming that such interpretation should only
290 bring indications about how diffusive transport is impaired.

291 3. RESULTS

292 3.1. μCT imaging of the barite precipitate

293 The μCT image of the chalk sample (obtained after 140 days) reported in **Figure 1A** shows that
294 barite precipitates form a thin reacted zone in the center of the sample. For kaolinite, the μCT
295 images reported in **Figure 1B** (obtained after 30 days) and **Figure 1C** (obtained after 60 days)
296 show spherical barite precipitates evenly distributed in the reacted zone which is further slightly
297 shifted towards barium inlet surface. The shifting of the precipitated zone might be due combined
298 effect of barium sorption on kaolinite pore surface (barium distribution coefficient, K_D , obtained
299 from batch experiments is equal to $3 \times 10^{-3} \text{ m}^3 \text{ kg}^{-1}$, see supporting information) and smaller
300 self-diffusion coefficient in water of Ba^{2+} compared to SO_4^{2-} ions ($D_{0, \text{Ba}^{2+}} = 8.5 \times 10^{-10} \text{ m}^2 \text{ s}^{-1}$
301 vs $D_{0, \text{SO}_4^{2-}} = 10.7 \times 10^{-10} \text{ m}^2 \text{ s}^{-1}$, Li and Gregory, 1973). Because the scan resolution ($16 \mu\text{m}$) is
302 much larger than the mean size of pores, each of the spheres in reality represents a cluster of

303 small barite precipitates distributed within the matrix (see Figure S4 in the supporting
304 information for SEM images acquired from a similar study).

305 **3.2 Diffusion of HTO and $^{36}\text{Cl}^-$ through intact materials**

306 The activity data for HTO for intact chalk sample have been already reported in Rajyaguru et
307 al. (2019). These authors estimated a value of $D_{e, \text{HTO}, \text{chalk}}$ equal to $41.5 \times 10^{-11} \text{ m}^2 \text{ s}^{-1}$. The
308 modeled experimental curve for HTO at intact conditions is reported in **Figure 2A** for
309 comparison with the reacted conditions. We must recall that the chalk sample at intact conditions
310 is composed of large pore volumes with pore throat of 660 nm. At intact conditions, it can be
311 assumed that the effect of the chalk surface charge would be negligible on diffusivity of $^{36}\text{Cl}^-$
312 ion. Moreover, the self-diffusion coefficient of $^{36}\text{Cl}^-$ in water is slightly lower than HTO (Li and
313 Gregory, 1973) ($D_{0, \text{HTO}} = 2 \times 10^{-10} \text{ m}^2 \text{ s}^{-1}$ and $D_{0, 36\text{Cl}} = 1.7 \times 10^{-10} \text{ m}^2 \text{ s}^{-1}$ or $D_{0, \text{HTO}}/D_{0, 36\text{Cl}} =$
314 1.17). Using this relationship, the diffusivity coefficient of ^{36}Cl at intact conditions in chalk can
315 be assumed to be equal to $D_{e, 36\text{Cl}, \text{chalk}} = 35.3 \times 10^{-11} \text{ m}^2 \text{ s}^{-1}$. This value of effective diffusion
316 coefficient was then used in I-mode to calculate the modeled experimental curve of ^{36}Cl reported
317 in **Figure 2B** for comparison. For intact kaolinite, the experimental cumulative activity data
318 obtained for HTO and $^{36}\text{Cl}^-$ are reported in **Figure 2 (C&D)** and they were numerically
319 reproduced using I-Mode with $D_{e, \text{HTO}, \text{kaolinite}} = 29 \times 10^{-11} \text{ m}^2 \text{ s}^{-1}$ and $D_{e, 36\text{Cl}, \text{kaolinite}} = 24 \times 10^{-$
320 $11 \text{ m}^2 \text{ s}^{-1}$. The values of effective diffusion coefficient for HTO and $^{36}\text{Cl}^-$ are close to those
321 determined by Glaus *et al.* (2010) for the KGa-1b type of kaolinite at a dry density of
322 1900 kg m^{-3} . The small difference in the effective diffusion coefficient values ($D_{e, \text{HTO}}/D_{e, 36\text{Cl}} =$
323 1.20) for both species through intact kaolinite is within the expected limit. Thus, diffusive tests
324 show that both HTO and $^{36}\text{Cl}^-$ tracers have a similar diffusion rate through kaolinite at a dry

325 density of 1690 kg m^{-3} . Finally, a complete overview of diffusive parameters obtained at intact
326 conditions are summarized in **Table 1**.

327 **3.3. Diffusive property changes in chalk and kaolinite samples deduced from mass** 328 **balance calculations and tracer tests**

329 **Figure 3A** and **Figure 3B** show the concentration evolution of reactants in the upstream and
330 downstream reservoirs of cells CHA-A and KAO-A. In both cases, barium and sulfate ions were
331 not detected in their counter reservoirs and were not reported in these figures. Since the solubility
332 of barite is very low ($K_{sp}^{\text{(barite)}} = 10^{-9.97}$) (Putnis *et al.*, 1995), the supersaturation to initiate
333 precipitation (around 10^{-4} to $10^{-5} \text{ mol L}^{-1}$ of equal barium and sulfate concentrations) is easily
334 reached. At this stage, most of barium and sulfate ions would have participated in barite
335 precipitation, resulting in a porosity reduction in both samples. After 140 days of experiment,
336 based on the barium concentration evolution in reservoirs, the amount of barium contributing to
337 barite precipitation in chalk and kaolinite was equal to 2.7 mmol and 0.04 mmol, respectively.
338 Using (i) a molar volume of $52.1 \text{ cm}^3 \text{ mol}^{-1}$ for barite and (ii) the initial porosity, the volume
339 occupied by barite in chalk was 0.14 cm^3 corresponding to overall 2.5 % decrease in porosity at
340 sample scale. Similarly, for the kaolinite experiment, barite precipitates occupied 0.0021 cm^3
341 corresponding to an overall 0.5 % decrease in porosity (Table S3 in supporting information).

342 To assess the impact of precipitation on diffusivity, tracers' tests were carried out for the
343 kaolinite experiment once reservoir monitoring confirmed that quasi-equilibrium state was
344 reached, *i.e.*, after 85 days, and for chalk experiment after 300 days (**Figure 2**). For chalk, barite
345 precipitation led to a significant decrease of HTO and $^{36}\text{Cl}^-$ diffusivity values with
346 $D_{e, \text{HTO}, \text{chalk}} = 13.5 \times 10^{-11} \text{ m}^2 \text{ s}^{-1}$ and $D_{e, \text{36Cl}, \text{chalk}} = 1.1 \times 10^{-11} \text{ m}^2 \text{ s}^{-1}$ respectively (values
347 reported in **Table 1**). Similarly, for kaolinite, precipitation led to a HTO diffusivity decrease with

348 $D_{e, HTO, kaolinite} = 0.15 \times 10^{-11} \text{ m}^2 \text{ s}^{-1}$ and a total hindering of $^{36}\text{Cl}^-$ diffusion. The modeled
349 curves are reported in supporting information in Figure S5, and the associated diffusivity
350 coefficient values in supporting information in Table S2. The calculated porosity values along
351 with HTO diffusivity data showed that barite precipitation led to a more significant change in
352 kaolinite transport properties than for chalk.

353 **4. DISCUSSION**

354 **4.1. Pore structure driven barite precipitation and changes in sample transport properties**

355 In section 3.1, post-mortem characterization of chalk and kaolinite by μCT imaging showed two
356 distinct barite precipitate patterns. In chalk sample, evenly distributed barite precipitates formed a
357 thin wall at the center of the sample, whereas in kaolinite sample the barite precipitates formed
358 evenly distributed isolated clusters over a broad zone in the center of the sample. Due to the
359 sample geometry and adopted experimental approach, it was not possible to quantify how these
360 precipitates evolved over time at pore scale. Nevertheless, observations from recent literature
361 connected to present work can allow us to decipher key parameters governing distinct barite
362 precipitation in chalk and kaolinite samples.

363 A study dealing with barite precipitation in compacted sand sample showed that barite would
364 precipitate with two different growth rates in different pore volumes (Poonoosamy *et al.*, 2015).
365 Indeed these growth behaviors also controlled their final morphology and distribution in
366 compacted sand samples (Poonoosamy *et al.*, 2016). This study showed micro-crystalline barite
367 precipitate growth in larger pore volumes (100 μm) and nano-crystalline barite precipitates
368 growth on the small pore walls (10 μm). The micro-crystalline barite precipitated with a growth
369 rate of $3.9 \times 10^{-13} \text{ m}^2 \cdot \text{s}^{-1}$ whereas nano-crystalline barite precipitated with a growth rate of
370 $2.7 \times 10^{-12} \text{ m}^2 \cdot \text{s}^{-1}$. Indeed the supersaturation threshold to initiate micro-crystalline barite
371 precipitation was equal to 4.08, whereas nano-crystalline barite precipitated at a lower

372 supersaturation threshold value equal to 3.6 respectively (Prasianakis *et al.*, 2017). These
373 calculations were based on classical nucleation theory that states that mineral forming from pore
374 solution grows *via* homogeneous nucleation and mineral forming on a foreign substrate (pore
375 walls in this case) grows *via* heterogeneous nucleation. Classical nucleation theory states that a
376 mineral requires an interfacial energy to form stable precipitate as it grows on foreign substrate,
377 but mineral requires higher threshold energy to form from the pore solution (Kashchiev and van
378 Rosmalen, 2003; Nielsen and Sohnel, 1969). This interfacial energy is key to determine the
379 cluster of nuclei required to form a stable precipitate and a given mineral could obtain different
380 morphologies depending upon the nucleation path it undertakes to initiate precipitation (Henzler
381 *et al.*, 2018; Kawano *et al.*, 2009; Loste *et al.*, 2004; Prieto, 2014). These observations present a
382 direct link between pore volumes and mineral intrinsic property (solubility, growth rate)
383 controlling precipitation in a given pore size distribution.

384 In present study, barite precipitation was initiated through a counter diffusion setup where Ba^{2+}
385 ion from reservoir-1 and SO_4^{2-} ion from reservoir-2 would diffuse into the sample and
386 progressively increase their concentration into the sample pore solutions. Interaction of both ions
387 would supersaturate the pore solutions with respect to barite mineral in pores located in the “first
388 points of meeting”. Over passage of time as more and more Ba^{2+} and SO_4^{2-} would diffuse and
389 interact in these first points of meeting, they would increase the barite supersaturation in pore
390 volumes until a threshold is achieved from where barite precipitation could be initiated in these
391 pore volumes. As barite mineral starts to precipitate, it consumes significant amount of Ba^{2+} and
392 SO_4^{2-} ions from pore solution. The chalk sample in our study is a natural material and it has
393 larger heterogeneities in its pore structure. These heterogeneities will control the local diffusion
394 of ions from sample surface until the first points of meeting in the center of the sample generating
395 a slight variation in local supersaturation in pores. In the pores where threshold supersaturation is

396 achieved (depending upon their pore size), precipitation is initiated and the transport experiment
397 is no longer dependent upon pure diffusion. These first precipitates would reduce barium and
398 sulfate concentration in pore solutions and thus enhancing diffusion of these ions towards these
399 pores from neighboring pore solution leading to evolution of reacted front around these first
400 points of precipitation. Along with low solubility, barite also possess slow kinetics of
401 precipitation. As mean pore size of chalk sample is 660 nm a longer time is required to fill such
402 pores with barite mineral. This means that a concentration gradient between these pores of first
403 precipitation and neighboring pores continues for a longer time and Ba^{2+} and SO_4^{2-} diffusion is
404 restricted around these pores. It is for this reason most of the barite precipitation is restricted to
405 the center of the sample in chalk case.

406 The mean pore throat of kaolinite sample is 35 nm that is 19 times smaller than for chalk
407 sample. This means that once precipitation is initiated in pore volumes, it will take much shorter
408 time to fill these pore volumes than the large pore volumes in chalk case. These precipitates even
409 in small volumes would strongly reduce the pore size and generate partially filled pores where
410 surface charge effects between barite wall and kaolinite wall will start to become dominant for
411 ionic diffusion. Due to such restriction, there is no further concentration gradient possible
412 between these pore volumes and neighboring pore volumes and resulting in pore connectivity
413 loss. Thus, Ba^{2+} and SO_4^{2-} ions will need to find another pathway to meet and supersaturate pore
414 solution to initiate precipitation. The low solubility of barite will ensure that supersaturation in
415 such other places is easily achieved. As more and more of such pores are filled, all the possible
416 pore connectivity allowing Ba^{2+} and SO_4^{2-} to meet and supersaturate pore solution is completely
417 restricted. Finally, the evolution of this system should stop connected pathways required for SO_4^{2-}
418 to diffuse and meet Ba^{2+} to supersaturate the pore solutions. Such sharper pore filling also
419 resulted in broader precipitation front where precipitates are evenly distributed. It is noteworthy

420 that the reliability of this hypothesis can only be fully assessed by performing a rather advanced
421 modelling incorporating all these coupled mechanisms, which is out of the scope of this study.

422 The diffusion tests conducted before and after precipitation experiments showed that generation
423 of barite precipitated zone had distinct impact on transport properties of chalk and kaolinite
424 samples.

425 In chalk, this precipitation process led to HTO diffusivity decrease by a factor of 2 and $^{36}\text{Cl}^-$
426 diffusivity decrease by a factor of 30. To further analyze the impact of pore connectivity loss on
427 global transport properties of samples, let us consider the chalk reacted zone thickness equal to
428 500 μm , with maximum and minimum thicknesses of 1 mm and 300 μm , respectively. Similarly,
429 the thickness of barite reacted zone in kaolinite sample is approximately equal to 2 mm, with
430 maximum and minimum thicknesses equal to 3 mm and 1 mm, respectively. These values were
431 estimated from μCT images and SEM observations (see Figure S2 and Figure S3 in the
432 supporting information). For each selected thickness, mass balance calculations were performed
433 to determine residual porosity in the reacted zones of chalk and kaolinite samples. The minimum
434 and maximum porosity reduction values for each case are also reported in **Table 1**. Considering
435 the mean experimental thickness, barite precipitation led to chalk porosity reduction from 45 % to
436 12 % and for kaolinite, porosity decreases from 36 % to 34.5 %, respectively. These data
437 apparently contradict the drastic drop of diffusivity in kaolinite considering the rather moderate
438 decrease of porosity in the reacted zone compared to chalk (**Table 1**).

439 To further discuss this point, we calculated the corresponding values of geometric factor, which
440 takes into account the effect of tortuosity and constrictivity of the pore space (**Table 1**) (the
441 concept of geometric factor and associated diffusivity calculations are explained in supporting
442 information). In chalk, barite precipitation decreased geometric factor of HTO by a factor of 8,
443 due to its limited diffusion through the remaining connected pore network in 12 % of residual

444 porosity. In this pore network, the partially filled pores with smaller diameter and strong EDL
445 effects between barite and chalk surface would further impose strong restricted $^{36}\text{Cl}^-$ diffusion. It
446 is for this reason barite precipitation led to decrease in geometric factor for $^{36}\text{Cl}^-$ by a factor of
447 115.

448 For kaolinite, mass balance calculations showed that barite precipitation resulted in 1.5 %
449 porosity decrease and 34.5 % residual porosity in reacted zone. However, diffusivity tests for
450 HTO show its diffusivity decrease by a factor of 200 and geometric factor decrease by a factor of
451 1000. These results show that the residual porosity in the reacted zone contains very small
452 connected network that would allow HTO diffusion. The partially filled pores in residual porosity
453 have very small pore sizes (< 35 nm) with strong charge effects between kaolinite and barite
454 surface. Thus, this connected network is not accessible for $^{36}\text{Cl}^-$ ion transport and resulting in its
455 complete diffusion restriction.

456 **4.2. Ionic transport alteration driven by local barite precipitation**

457 In previous section, we noted that barite precipitation led to generation of two distinct connected
458 network within the reacted zone. Each of this reacted zone contains: 1. Pore completely filled
459 with barite, 2a. Pore partially filled with small volume of barite, 2b. Pore filled with significant
460 volume of barite 3. Empty pores with no presence of barite.

461 The pores fully occupied with barite would correspond to dead-end pores through which no
462 diffusion could occur. The partially-filled pores with small and significant barite volumes along
463 with empty pores would account for pore connectivity in reacted zone and possible HTO and
464 $^{36}\text{Cl}^-$ diffusion.

465 Since, diffusion tests showed contradictory diffusive behavior of both tracers through reacted
466 zones of chalk and kaolinite sample, the simple 1D diffusion equation (reported in section 2.5) is

467 unable to explain underlying causes for contradictory diffusion behavior of HTO and ^{36}Cl before
468 and after precipitation process. Moreover, the water layer adjacent to mineral surface generates
469 electric double layer of either negative or positive charge. Depending on the charge of this
470 surface and that of the ions, the diffusion of the ions may be retarded (Appelo and Wersin, 2007;
471 Sposito, 2008; Stumm and Morgan, 2012). Moreover, natural chalk materials and kaolinite are
472 also known to present surface charge at full water saturation conditions (Al Mahrouqi *et al.*,
473 2017; Alkan *et al.*, 2005). In present study, depending upon the size of newly formed residual
474 pore volumes, the thickness of free water layer would vary and it is sandwiched in between newly
475 formed surfaces composed of either barite/barite, barite/chalk, or barite/kaolinite respectively.
476 Barite mineral surface charge can be controlled and even reversed by varying pH, ionic strength
477 and by increasing the presence of potential determining ions (PDI^s) such as Ba^{2+} and SO_4^{2-}
478 (Bokern *et al.*, 2003; Hang *et al.*, 2007). Depending upon the local pore chemistry, each pore
479 volume could either possess positive surface charge where $^{36}\text{Cl}^-$ diffusion could be retarded or
480 negative surface charge which could inhibit $^{36}\text{Cl}^-$ diffusion. Indeed the strength of these surface
481 charges depend upon the pore size, local ionic strength and presence of potential determining
482 ions. Thus, combination of these pore volumes generate a residual pore size distribution with
483 varying electric double layer thickness and surface charge in each pore. Indeed, the theoretical
484 and experimental works carried by (Muniruzzaman and Rolle, 2019; Soler *et al.*, 2019;
485 Tournassat and Steefel, 2015) show that such varying pore volumes clearly control the nature of
486 cationic and anionic species transport.

487 To explore such surface charge effects on ion mobility, electrophoretic mobility using zeta
488 potential measurements was determined in the current study on chalk, kaolinite and barite powder
489 under the different pore chemistry found in our reactive experiments. For that purpose, barium or

490 sulfate was added in chalk or kaolinite pore water solutions at a concentration varying from 10^{-5}
491 mol L^{-1} to $10^{-2} \text{mol L}^{-1}$. These values were chosen assuming that, when HTO and $^{36}\text{Cl}^{-}$
492 diffusion tests are launched, the reacted zone can be then divided into two main zones. The first
493 zone (called Zone-Ba) would contain precipitates that are equilibrated with pore solution
494 containing an excess of barium ions that cannot easily diffuse anymore through the reacted zone.
495 In this case, one can assume that the barium concentration value would be close to the value
496 measured in the upstream reservoir when the quasi-equilibrium is reached, *i.e.*, $ca 5 \times 10^{-3}$ and ca
497 $1.5 \times 10^{-3} \text{mol L}^{-1}$ in chalk or kaolinite experiments, respectively (**Figure 3**). Similarly,
498 precipitates in second zone (called Zone-SO₄) would be equilibrated with pore solution
499 containing an excess of sulfate ions, with concentrations close to $ca 1 \times 10^{-3}$ and $ca 1.5 \times 10^{-3}$
500 mol L^{-1} in chalk or kaolinite experiments, respectively (**Figure 3**). Conversely, sulfate or barium
501 concentrations in Zone-Ba or Zone-SO₄ (resp.) should be controlled by the barite solubility at a
502 value close to $10^{-5} \text{mol L}^{-1}$. For each case, three replicates of batch experiments were prepared,
503 consisting of 0.06 g of mineral powder suspended in 9 mL of pore water. The suspended solution
504 was equilibrated by shaking tube for 15 hours. Finally, 1 mL of solution was injected in
505 zetameter setup (labelled Zetasizer Nano from Malvern Panalytical) and the evolution of zeta
506 potential was measured with the mean acquisition time of 2-3 minutes. For chalk or barite
507 powder suspended in chalk pore water, the pH was equal to 7.6 or 7.2, respectively. For kaolinite
508 or barite suspended in kaolinite pore water the pH was equal to 5.8 or 5.5, respectively. Zeta
509 potential results reported in **Figure 4** indicate that barite powder showed positive zeta potential
510 values under all the experimental conditions, except in the case of sulfate concentration greater
511 than $10^{-3} \text{mol L}^{-1}$ in chalk pore water. Chalk powder surface was always negatively charge,

512 independently of the reactant concentration, while kaolinite was mainly under negative form,
513 except for barium concentration higher than 10^{-3} mol L⁻¹.

514 Based on these data and on how barite precipitation mechanisms can occur in confined pores, we
515 propose a schematic representation of newly formed surfaces in the reacted zone and their
516 possible impact of solute diffusion (**Figure 5**). Case-1 concerns large pores completely filled with
517 barite mineral in chalk sample. These pores contribute as dead end pores and contribute to no
518 diffusion of both HTO and ³⁶Cl.

519 Case-2 deals with smaller pores found both in chalk and kaolinite materials where barite
520 precipitation has occurred on the kaolinite/chalk pore surface. In Case-2A, barite overgrowth
521 partially masks/covers the initial material. For chalk, Case-2A(Cha) shows two possible scenarios
522 where one side of pore composed of chalk surface will always maintain negative surface charge.
523 The other side of pore surface is composed of barite of either negative or positive surface charge
524 (depending upon PDIs concentration). In contrast, Case-2A(Kao) shows pores composed on one
525 side with positively charged kaolinite surface and on other side with either negatively or
526 positively charged barite surface. Both of these cases clearly show the distinct evolution of
527 surface charge properties for barite precipitation in kaolinite and chalk samples. Finally, barite
528 overgrowth can also completely cover the pore surface and would remain in direct contact with
529 the remaining pore water (Case2B). Thus, in such pores for both chalk and kaolinite case, the
530 PDIs would control barite surface charge that, in turn, governs the nature of ionic transport. Both
531 of Case-1 and Case-2(A,B) could explain the selective restriction of anionic species transport
532 through the reacted zones of chalk and kaolinite samples. Nevertheless, as kaolinite pore volumes
533 are much smaller compared to chalk, barite precipitation would significantly reduce the diameter
534 of these pores. Thus, the newly formed surface charge properties in Case2A(Kao) and

535 Case2B(Kao) would have a much more pronounced effect on ionic transport in the kaolinite case.
536 These considerations may satisfactorily explain the reduction of $^{36}\text{Cl}^-$ diffusivity in chalk and its
537 complete restriction in kaolinite after the occurrence of clogging phenomenon.

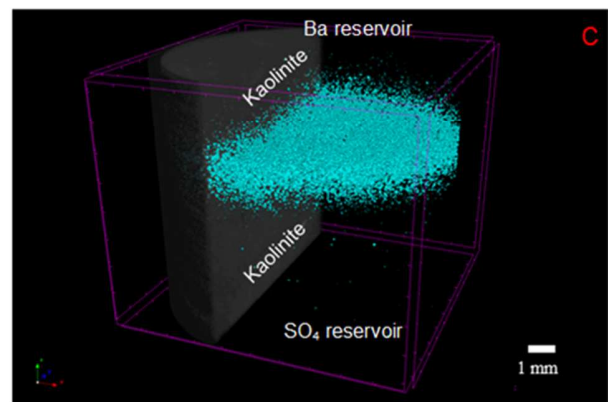
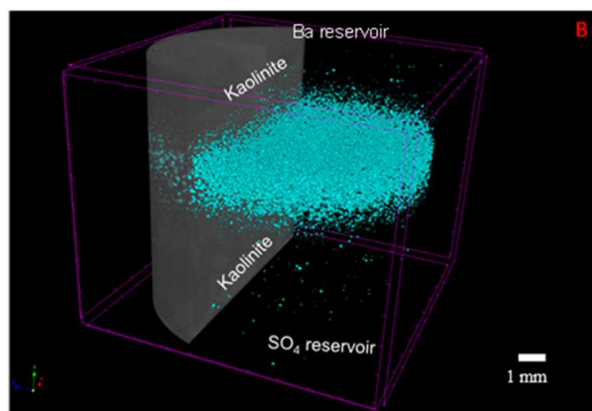
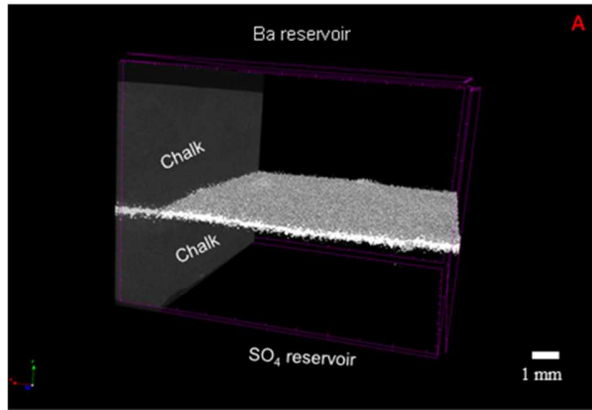
538 In the future course of this project, dedicated complementary post-mortem analyses such as FIB-
539 SEM, XRF/XRD measurements are planned to be carried out to determine precipitates
540 morphology in pores smaller than 50 nm with possibility of determining concentration of residual
541 ionic species. Such investigation would further bring in new arguments to quantify the analysis
542 presented in this work. The experimental results presented in this work also highlight the
543 limitation of simple diffusion equation (reported in section 2.5) without taking into account EDL
544 effects. To quantify such effects, surface charge behavior of barite/barite, barite/chalk,
545 barite/kaolinite with varying free water thickness pH, IS, and potential determining ion
546 concentrations is being studied using a multi-component diffusion theory. The authors believe
547 that such numerical task in future scope of work will further strengthen arguments presented in
548 this article.

549 **5. CONCLUSIONS**

550 The present study aimed at understanding pore scale clogging mechanism under diffusive
551 controlled transport regime. It is expected that such process would affect containment properties
552 of natural rocks that are envisaged (i) to host deep geological facilities for radioactive waste
553 storage or (ii) as cap rocks for global carbon sequestration.

554 The investigation of barite precipitation in chalk and compacted kaolinite samples showed that in
555 a diffusion-controlled transport, pore size distribution is key in controlling the initiation points of
556 precipitation. These points of initiation would then determine the final pattern of reacted zone and
557 generate a unique feedback on transport properties of the porous sample. Moreover, the
558 electrophoretic measurements also showed that pH and PDI^s can have a tremendous influence on
559 transport of ionic species. During clogging process, the emerging local chemical complexities
560 (mineral distribution, mineral surface charge) could then potentially change the nature of ionic
561 transport through the newly formed reacted zone. The experiments performed with two different
562 materials evidenced that clogging was mainly driven by local physicochemical process (pore
563 structure effects combined with mineral reactivity). In this case, averaged porosity loss alone in
564 clogged zone is not sufficient to determine the alteration extent of rock transport properties. The
565 present work therefore shows that the applicability of relationships such as Archie's law is
566 limited in this context and that there is a need to quantify the nature of clogging in porous
567 material of varying physical complexities and under varying chemical complexities.

568



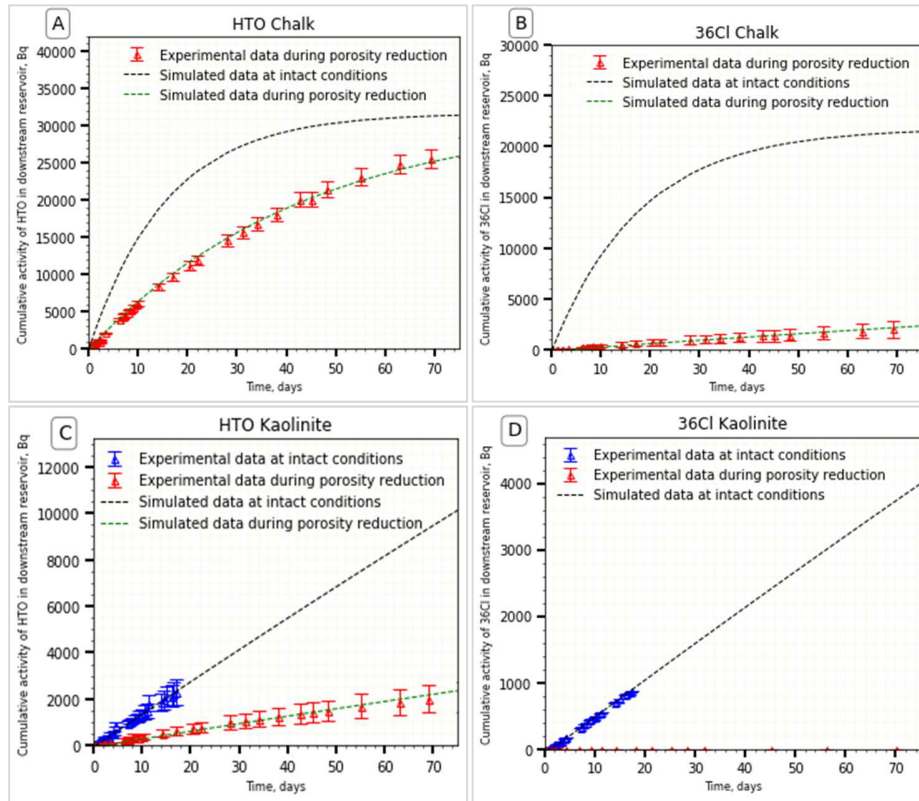
569

570 **Figure 1.** (A) μ CT images of barite precipitation zone (in grey) formed at the center of the chalk

571 sample between two intact matrices. (B, C) μ CT images of kaolinite sample in which formation

572 of barite precipitates clusters (blue) are observed after 30 days (B) and after 60 days (C).

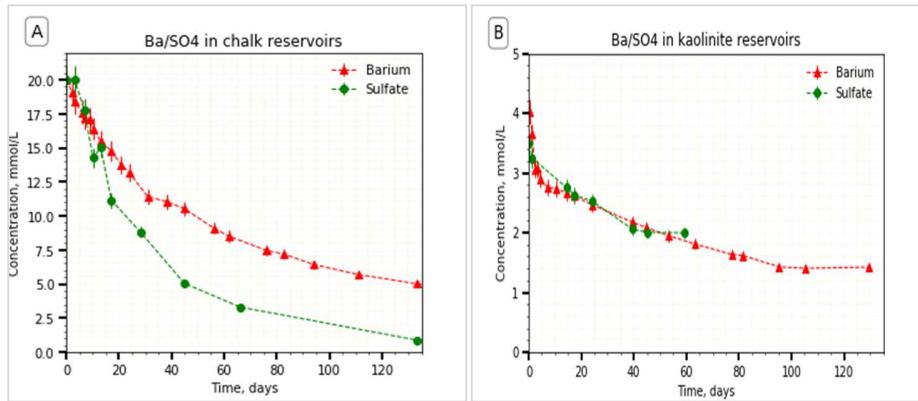
573



574

575 **Figure 2.** Results of diffusion experiment. (A&B) Chalk: Evolution of HTO and ³⁶Cl cumulative
576 activity during porosity reduction by barite precipitation, (C & D), Kaolinite: Evolution of HTO
577 and ³⁶Cl cumulative activity prior to and during porosity reduction by barite precipitation. The
578 modeled activity curves for intact sample and reacted sample are presented in blue and green
579 (resp.), using I-mode and values of the diffusive parameters reported in **Table 1**.

580



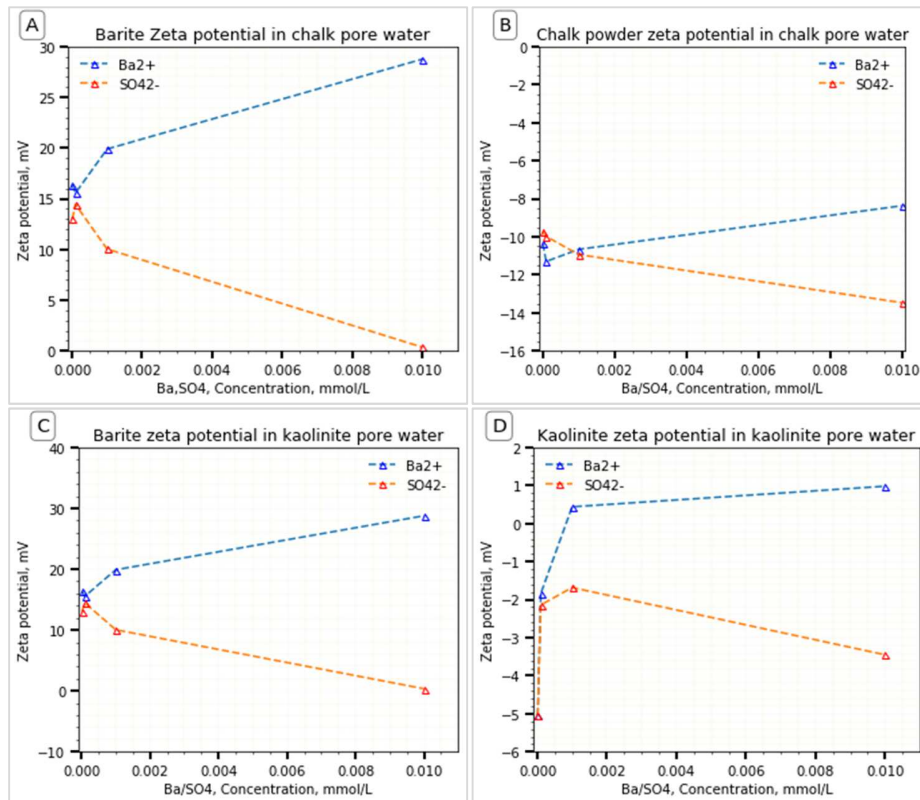
581

582 **Figure 3.** Concentration evolution of Ba²⁺ (in upstream reservoir) and SO₄²⁻ (in downstream

583 reservoir) as a function of time in CHA-A cell (A) and KAO-A cell (B) (chalk results were

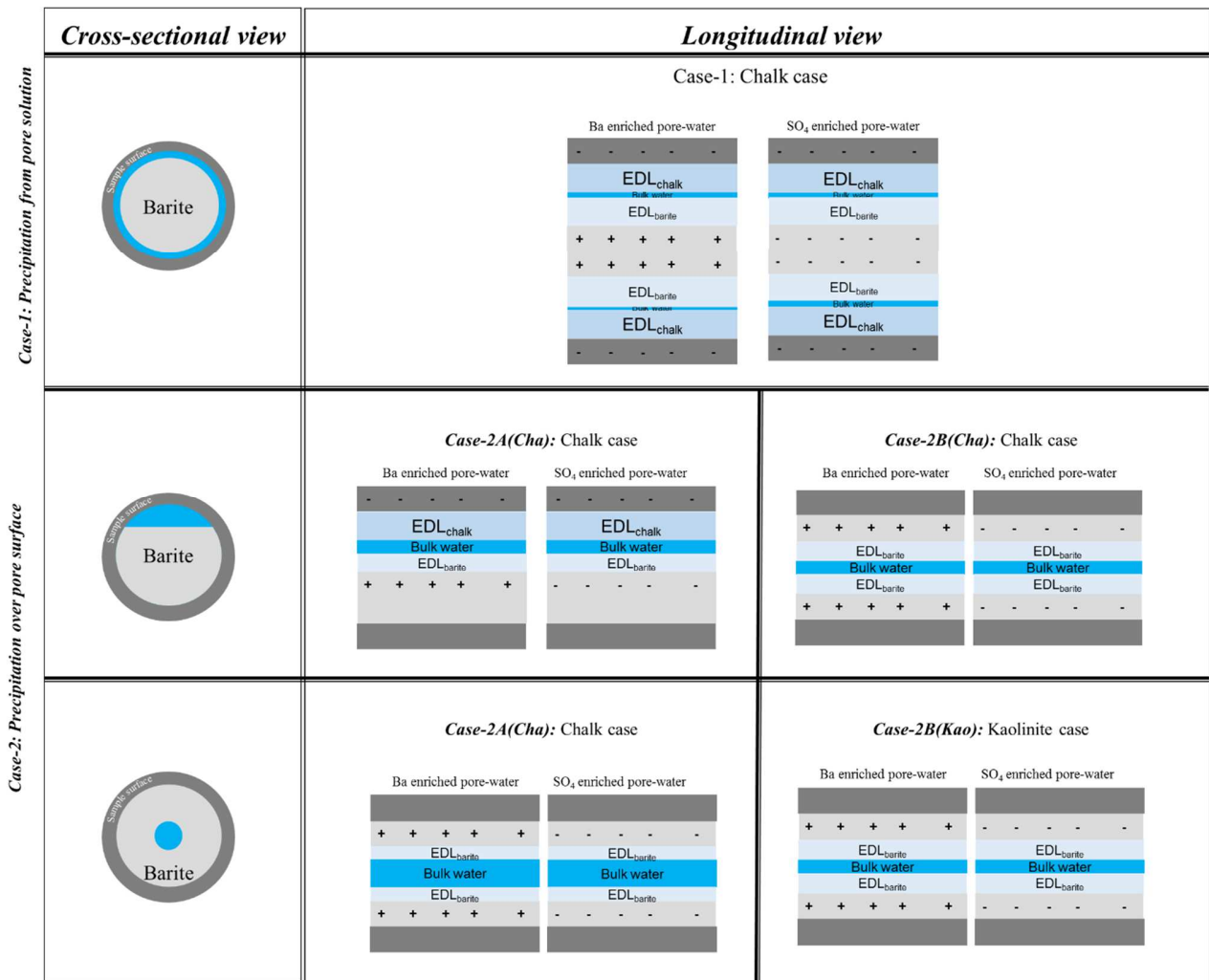
584 obtained in Rajyaguru *et al.* (2019))

585



586
587

Figure 4. (A) Evolution of barite powder zeta potential in chalk pore water. (B) Evolution of
588 chalk powder zeta potential in chalk pore water. (C) Evolution of barite powder zeta potential in
589 kaolinite pore water. (D) Evolution of kaolinite powder zeta potential in kaolinite pore water. All
590 measurements were carried out in presence of either Ba²⁺ and SO₄²⁻ and of concentration varying
591 in range between 10⁻⁵ mol L⁻¹ to 10⁻² mol L⁻¹.



592

593 **Figure 5.** Schematic view of different pore structures resulting from nucleation driven barite

594 precipitation. The combination of barite morphology (light-grey) and host surface geometry

595 (dark-grey) along with barium and sulfate pore concentrations generates different possibilities of

596 pore surface charge properties. Dark-blue corresponds to bulk water, while light-blues correspond

597 to the part of the pore submitted to the effect of mineral surface with the presence of an electric

598 double layer (EDL_{barite}, EDL_{chalk} or EDL_{kaolinite}).

599 **Table 1.** Porosities, effective diffusion coefficient and geometric factor values for HTO and $^{36}\text{Cl}^-$
 600 calculated for an intact sample, a whole reacted sample and the reacted zone.

		Porosity %	$D_{e,\text{HTO}} \times 10^{-11}$ $\text{m}^2 \cdot \text{s}^{-1}$	$D_{e,^{36}\text{Cl}} \times 10^{-11}$ $\text{m}^2 \cdot \text{s}^{-1}$	G_{HTO} (-)	$G_{^{36}\text{Cl}}$ (-)
Chalk	Intact material	45	41.5	35.3	0.46	0.46
	Whole sample (6.5 mm)	42.5	13.5 (11.5 - 17.5)	1.1 (0.9 - 1.3)	0.16	0.015
	Reacted zone 500 μm (300 μm- 1 mm)	12 (4 - 28.5)	1.48 (0.060 - 4.20)	0.08 (0.04 - 0.25)	0.060	0.004
Kaolinite	Intact material	36	29	23	0.4	0.40
	Whole sample (10 mm)	35.5	0.15 (0.06 - 0.21)	(N/A)	0.002	N/A
	Reacted zone 2 mm (1 - 3 mm)	34.5 (32 - 35)	0.03 (0.01 - 0.05)	(N/A)	0.0004	N/A

601

602

603 **REFERENCES**

- 604 Al Mahrouqi, D., Vinogradov, J., Jackson, M.D., 2017. Zeta potential of artificial and natural
605 calcite in aqueous solution. *Adv. Colloid Interface Sci.* 240, 60–76.
606 <https://doi.org/10.1016/j.cis.2016.12.006>
- 607 Alkan, M., Demirbaş, Ö., Doğan, M., 2005. Electrokinetic properties of kaolinite in mono- and
608 multivalent electrolyte solutions. *Microporous Mesoporous Mater.* 83, 51–59.
609 <https://doi.org/10.1016/j.micromeso.2005.03.011>
- 610 Altmann, S., Tournassat, C., Goutelard, F., Parneix, J.-C., Gimmi, T., Maes, N., Bensenouci, F.,
611 Appelo, C.A.J., Wersin, P., Oelkers, E.H., Lasaga, A.C., Horseman, S.T., Higgo, J.J.W.,
612 Alexander, J., Harrington, J.F., Fatnassi, I., Emmanuel, S., Ague, J.J., Walderhaug, O.,
613 Chagneau, A., Bosbach, D., Wood, S.A., Berthe, G., Putnis, A., Prieto, M., Fernandez-Diaz,
614 L., Mauthe, G., Prieto, M., Fernández-Díaz, L., López-Andrés, L., López-Andrés, S.,
615 Poonosamy, J., Mäder, U., Palandri, J.L., Kharaka, Y.K., Steefel, C.I., Sposito, G., Savoye,
616 S., Sangwal, K., Treybal, R., Tournassat, C., Steefel, C.I., Appelo, C.A.J., 2015. Impact of
617 porosity variation on diffusive transport: experimentation vs simulation. *Geochim.*
618 *Cosmochim. Acta* 1, 447–460.
- 619 Andra, 2005. Dossier 2005 Argile - Synthèse Evaluation de la faisabilité du stockage géologique
620 en formation argileuse 240.
- 621 Appelo, C.A.J., Wersin, P., 2007. Multicomponent diffusion modeling in clay systems with
622 application to the diffusion of tritium, iodide, and sodium in opalinus clay. *Environ. Sci.*
623 *Technol.* 41, 5002–5007.
- 624 Archie, G.E., 1942. The Electrical Resistivity Log as an Aid in Determining Some Reservoir

625 Characteristics. *Trans. AIME* 146, 54–62. <https://doi.org/10.2118/942054-G>

626 Bachu, S., 2002. Sequestration of CO₂ in geological media in response to climate change: Road
627 map for site selection using the transform of the geological space into the CO₂ phase space.
628 *Energy Convers. Manag.* 43, 87–102. [https://doi.org/10.1016/S0196-8904\(01\)00009-7](https://doi.org/10.1016/S0196-8904(01)00009-7)

629 Bazer-Bachi, F., Tevissen, E., Descostes, M., Grenut, B., Meier, P., Simonnot, M.O., Sardin, M.,
630 2006. Characterization of iodide retention on Callovo-Oxfordian argillites and its influence
631 on iodide migration. *Phys. Chem. Earth* 31, 517–522.
632 <https://doi.org/10.1016/j.pce.2006.04.015>

633 Berthe, G., Savoye, S., Wittebroodt, C., Michelot, J.L., 2011. Changes in containment properties
634 of claystone caprocks induced by dissolved CO₂ seepage. *Energy Procedia* 4, 5314–5319.
635 <https://doi.org/10.1016/j.egypro.2011.02.512>

636 Besançon, C., Chautard, C., Beaucaire, C., Savoye, S., Sardini, P., Gérard, M., Descostes, M.,
637 2020. The role of barite in the post-mining stabilization of radium-226: A modeling
638 contribution for sequential extractions. *Minerals* 10, 1–21.
639 <https://doi.org/10.3390/min10060497>

640 Bokern, D.G., Hunter, K.A., McGrath, K.M., 2003. Charged Barite - Aqueous Solution
641 Interface: Surface Potential and Atomically Resolved Visualization. *Langmuir* 19, 10019–
642 10027. <https://doi.org/10.1021/la0269255>

643 Brandt, F., Klinkenberg, M., Poonosamy, J., Weber, J., Bosbach, D., 2018. The effect of ionic
644 strength and Sraq upon the uptake of Ra during the recrystallization of barite. *Minerals* 8.
645 <https://doi.org/10.3390/min8110502>

646 Chagneau, A., Claret, F., Enzmann, F., Kersten, M., Heck, S., Madé, B., Schäfer, T., 2015a.
647 Mineral precipitation-induced porosity reduction and its effect on transport parameters in
648 diffusion-controlled porous media. *Geochem. Trans.* 16, 1–16.
649 <https://doi.org/10.1186/s12932-015-0027-z>

650 Chagneau, A., Tournassat, C., Steefel, C.I., Bourg, I.C., Gaboreau, S., Esteve, I., Kupcik, T.,
651 Claret, F., Schäfer, T., 2015b. Complete restriction of ^{36}Cl -diffusion by celestite
652 precipitation in densely compacted illite. *Environ. Sci. Technol. Lett.* 2, 139–143.
653 <https://doi.org/10.1021/acs.estlett.5b00080>

654 Chautard, C., Beaucaire, C., Gerard, M., Roy, R., Savoye, S., Descostes, M., 2020. Geochemical
655 characterization of uranium mill tailings (Bois Noirs Limouzat, France) highlighting the U
656 and ^{226}Ra retention. *J. Environ. Radioact.* 218.
657 <https://doi.org/10.1016/j.jenvrad.2020.106251>

658 Crank, J., 1975. *The Mathematics of Diffusion*, 2nd ed. Oxford.

659 Dagnelie, R.V.H., Arnoux, P., Enaux, J., Radwan, J., Nerfie, P., Page, J., Coelho, D., Robinet,
660 J.C., 2017. Perturbation induced by a nitrate plume on diffusion of solutes in a large-scale
661 clay rock sample. *Appl. Clay Sci.* 141, 219–226. <https://doi.org/10.1016/j.clay.2017.02.025>

662 De Windt, L., Marsal, F., Tinseau, E., Pellegrini, D., 2008. Reactive transport modeling of
663 geochemical interactions at a concrete/argillite interface, Tournemire site (France). *Phys.*
664 *Chem. Earth* 33, 295–305. <https://doi.org/10.1016/j.pce.2008.10.035>

665 Descostes, M., Pili, E., Felix, O., Frasca, B., Radwan, J., Juery, A., 2012. Diffusive parameters of
666 tritiated water and uranium in chalk. *J. Hydrol.* 452–453, 40–50.

667 <https://doi.org/10.1016/j.jhydrol.2012.05.018>

668 Didierjean, S., Maillet, D., Moyne, C., 2004. Analytical solutions of one-
669 dimensional macrodispersion in stratified porous media by the quadrupole method:
670 convergence to an equivalent homogeneous porous medium. *Adv. Water Resour.* 27, 657–
671 667

672 Emmanuel, S., Ague, J.J., Walderhaug, O., 2010. Interfacial energy effects and the evolution of
673 pore size distributions during quartz precipitation in sandstone. *Geochim. Cosmochim. Acta*
674 74, 3539–3552.

675 Fleury, M., Brosse, E., 2018. Transport in Tight Rocks. *Geol. Carbon Storage Subsurf. Seals*
676 *Caprock Integr.* 238, 31.

677 Gaucher, E., Robelin, C., Matray, J.M., Négrel, G., Gros, Y., Heitz, J.F., Vinsot, A., Rebours, H.,
678 Cassagnabère, A., Bouchet, A., 2004. ANDRA underground research laboratory:
679 Interpretation of the mineralogical and geochemical data acquired in the Callovian-
680 Oxfordian formation by investigative drilling. *Phys. Chem. Earth* 29, 55–77.
681 <https://doi.org/10.1016/j.pce.2003.11.006>

682 Glaus, M.A., Frick, S., Rossé, R., Loon, L.R.V., 2010. Comparative study of tracer diffusion of
683 HTO, $^{22}\text{Na}^+$ and $^{36}\text{Cl}^-$ in compacted kaolinite, illite and montmorillonite. *Geochim.*
684 *Cosmochim. Acta* 74, 1999–2010. <https://doi.org/10.1016/j.gca.2010.01.010>

685 González-Caballero, F., Cabrerizo, M.A., Bruque, J.M., Delgado, A., 1988. The zeta potential of
686 celestite in aqueous electrolyte and surfactant solutions. *J. Colloid Interface Sci.* 126, 367–
687 370. [https://doi.org/10.1016/0021-9797\(88\)90131-2](https://doi.org/10.1016/0021-9797(88)90131-2)

688 Hang, J., Shi, L., Feng, X., Xiao, L., 2009. Electrostatic and electrosteric stabilization of aqueous
689 suspensions of barite nanoparticles. *Powder Technol.* 192, 166–170.
690 <https://doi.org/10.1016/j.powtec.2008.12.010>

691 Hang, J.Z., Zhang, Y.F., Shi, L.Y., Feng, X., 2007. Electrokinetic properties of barite
692 nanoparticles suspensions in different electrolyte media. *J. Mater. Sci.* 42, 9611–9616.
693 <https://doi.org/10.1007/s10853-007-1974-2>

694 Henzler, K., Fetisov, E.O., Galib, M., Baer, M.D., Legg, B.A., Borca, C., Xto, J.M., Pin, S.,
695 Fulton, J.L., Schenter, G.K., Govind, N., Ilja Siepmann, J., Mundy, C.J., Huthwelker, T., De
696 Yoreo, J.J., 2018. Supersaturated calcium carbonate solutions are classical. *Sci. Adv.* 4, 1–
697 12. <https://doi.org/10.1126/sciadv.aao6283>

698 Kashchiev, D., van Rosmalen, G.M., 2003. Review: Nucleation in solutions revisited. *Cryst. Res.*
699 *Technol.* 38, 555–574. <https://doi.org/10.1002/crat.200310070>

700 Kawano, J., Shimobayashi, N., Miyake, A., Kitamura, M., 2009. Precipitation diagram of
701 calcium carbonate polymorphs: Its construction and significance. *J. Phys. Condens. Matter*
702 21. <https://doi.org/10.1088/0953-8984/21/42/425102>

703 Li, Y.-H., Gregory, S., 1973. Diffusion of Ions in Sea Water and in Deep Sea Sediments.
704 *Geochim. Cosmochim. Acta*, 1974 38, 703–714. [https://doi.org/10.1016/0016-](https://doi.org/10.1016/0016-7037(74)90145-8)
705 [7037\(74\)90145-8](https://doi.org/10.1016/0016-7037(74)90145-8)

706 Loste, E., Park, R.J., Warren, J., Meldrum, F.C., 2004. Precipitation of calcium carbonate in
707 confinement. *Adv. Funct. Mater.* 14, 1211–1220. <https://doi.org/10.1002/adfm.200400268>

708 Mundhenk, N., Huttenloch, P., Sanjuan, B., Kohl, T., Steger, H., Zorn, R., 2013. Corrosion and

709 scaling as interrelated phenomena in an operating geothermal power plant. *Corros. Sci.* 70,
710 17–28. <https://doi.org/10.1016/j.corsci.2013.01.003>

711 Muniruzzaman, M., Rolle, M., 2019. Multicomponent Ionic Transport Modeling in Physically
712 and Electrostatically Heterogeneous Porous Media With PhreeqcRM Coupling for
713 Geochemical Reactions. *Water Resour. Res.* 55, 11121–11143.
714 <https://doi.org/10.1029/2019WR026373>

715 NAGRA, 2002. Project Opalinus Clay—Safety Report: Demonstration of disposal feasibility for
716 spent fuel, vitrified high-level waste and long-lived intermediate-level waste
717 (Entsorgungsnachweis). Wetingen, Switzerland.

718 Nielsen, A.E., Sohnel, O., 1969. Nucleation and Growth of Crystals at High Supersaturation.
719 *Krist. und Tech.* 4, 17–38. <https://doi.org/10.1002/crat.19690040105>

720 Poonoosamy, J., Curti, E., Kosakowski, G., Grolimund, D., Van Loon, L.R., Mäder, U., 2016.
721 Barite precipitation following celestite dissolution in a porous medium: A SEM/BSE and μ -
722 XRD/XRF study. *Geochim. Cosmochim. Acta* 182, 131–144.
723 <https://doi.org/10.1016/j.gca.2016.03.011>

724 Poonoosamy, J., Kosakowski, G., Van Loon, L.R., Mäder, U., 2015. Dissolution-precipitation
725 processes in tank experiments for testing numerical models for reactive transport
726 calculations: Experiments and modelling. *J. Contam. Hydrol.* 177–178, 1–17.
727 <https://doi.org/10.1016/j.jconhyd.2015.02.007>

728 Prasianakis, N.I., Curti, E., Kosakowski, G., Poonoosamy, J., Churakov, S. V., 2017.
729 Deciphering pore-level precipitation mechanisms. *Sci. Rep.* 7, 1–9.

730 <https://doi.org/10.1038/s41598-017-14142-0>

731 Prieto, M., 2014. Nucleation and supersaturation in porous media (revisited). *Mineral. Mag.* 78,
732 1437–1447. <https://doi.org/10.1180/minmag.2014.078.6.11>

733 Putnis, A., Mauthe, G., 2001. The effect of pore size on cementation in porous rocks. *Geofluids*
734 1, 37–41.

735 Putnis, A., Prieto, M., Fernandez-Diaz, L., 1995. Fluid supersaturation and crystallization in
736 porous media. *Geol. Mag.* 132, 1–13.

737 Radwan, J., Hanios, D., Grenut, B., 2006. Qualification expérimentale de la plate-forme
738 ALLIANCES . 1 ère Partie : Calculs préliminaires . GIF SUR YVETTE. <https://doi.org/NT>
739 DPC / SECR 06-051 indice A DO 190

740 Rajyaguru, A., L'Hôpital, E., Savoye, S., Wittebroodt, C., Bildstein, O., Arnoux, P., Detilleux,
741 V., Fatnassi, I., Gouze, P., V.Lagneau, 2019. Experimental characterization of coupled
742 diffusion reaction mechanisms in low permeability chalk. *Chem. Geol.* 503, 29–39.
743 <https://doi.org/S0009254118305199>

744 Rijniers, L.A., Huinink, H.P., Pel, L., Kopinga, K., 2005. Experimental evidence of
745 crystallization pressure inside porous media. *Phys. Rev. Lett.* 94, 23–26.
746 <https://doi.org/10.1103/PhysRevLett.94.075503>

747 Singurindy, O., Berkowitz, B., 2003. Evolution of hydraulic conductivity by precipitation and
748 dissolution in carbonate rock. *Water Resour. Res.* 39, 1–14.
749 <https://doi.org/10.1029/2001WR001055>

750 Soler, J.M., Steefel, C.I., Gimmi, T., Leupin, O.X., Cloet, V., 2019. Modeling the Ionic Strength

751 Effect on Diffusion in Clay. the DR-A Experiment at Mont Terri. ACS Earth Sp. Chem. 3,
752 442–451. <https://doi.org/10.1021/acsearthspacechem.8b00192>

753 Sposito, G., 2008. The chemistry of soils. Oxford university press.

754 Stumm, W., Morgan, J.J., 2012. Aquatic chemistry: chemical equilibria and rates in natural
755 waters. John Wiley & Sons.

756 Tertre, E., Savoye, S., Hubert, F., Prêt, D., Dabat, T., Ferrage, E., 2018. Diffusion of Water
757 through the Dual-Porosity Swelling Clay Mineral Vermiculite. Environ. Sci. Technol. 52,
758 1899–1907. <https://doi.org/10.1021/acs.est.7b05343>

759 Tournassat, C., Steefel, C.I., 2015. Ionic transport in nano-porous clays with consideration of
760 electrostatic effects. Rev. Mineral. Geochemistry 80, 287–329.

761 Vengosh, A., Jackson, R.B., Warner, N., Darrah, T.H., Kondash, A., 2014. A critical review of
762 the risks to water resources from unconventional shale gas development and hydraulic
763 fracturing in the United States. Environ. Sci. Technol. 48, 8334–8348.
764 <https://doi.org/10.1021/es405118y>

765 Vinograd, V.L., Kulik, D.A., Brandt, F., Klinkenberg, M., Weber, J., Winkler, B., Bosbach, D.,
766 2018. Thermodynamics of the solid solution - Aqueous solution system (Ba,Sr,Ra)SO₄ +
767 H₂O: I. The effect of strontium content on radium uptake by barite. Appl. Geochemistry 89,
768 59–74. <https://doi.org/10.1016/j.apgeochem.2017.11.009>

769

770